Effect of Reynolds Number on the Turbulent Flow Characteristics of Offset Synthetic Jets

Keziah N.D Hammond
Department of Mechanical, Industrial and Aerospace Engineering
Concordia University
1455 De Maisonneuve Blvd. West,
Montreal, Quebec
h_keziah@live.concordia.ca

Jessica Meilleur
Department of Mechanical, Industrial and Aerospace Engineering
Concordia University
1455 De Maisonneuve Blvd. West,
Montreal, Quebec
j_meil@live.concordia.ca

Ebenezer E. Essel
Department of Mechanical, Industrial and Aerospace Engineering
Concordia University
1455 De Maisonneuve Blvd. West,
Montreal, Quebec
ebenezer.essel@concordia.ca

ABSTRACT

This study investigates the influence of Reynolds number on the unsteady flow characteristics of offset synthetic jets (OSJs) using improved delayed detached eddy simulations (IDDES). Numerical simulations were performed at a fixed offset height ratio of $G/d = 2$ and actuation frequency of $300\ Hz$ for five Reynolds numbers, $Re = 280, 570, 840, 1000$, and 1230, based on the average jet-exit velocity and nozzle diameter. Phase-averaged, and time-averaged turbulent statistics, Q-criterion, and turbulent–non-turbulent interface (TNTI) are used to characterize the Reynolds number effects. Increasing Reynolds number enhances jet momentum, promoting earlier wall attachment, stronger entrainment, and more rapid vortex breakdown, from coherent axisymmetric rings at low Re to rapidly disintegrating small-scale worm-like structures at high Re. The velocity decay rate decreases from $n = 1.3$ at $R280$ to $n = 0.73$ at $R1000$. TNTI analysis reveals a transition from intermittent, vortex-ring-driven entrainment at low Re to a sustained broadband turbulent process at high Re. Conditional averaging based on the TNTI shows that peaks in streamwise velocity and turbulent kinetic energy occur near the interface at $R280$ and shift toward the turbulent core and wall at higher Reynolds numbers, consistent with stronger wall interactions.

INTRODUCTION

Synthetic jets (SJs) are zero-net-mass-flux jets generated by periodic suction and expulsion of fluid through an orifice, producing coherent vortical structures that interact strongly with the surrounding flow (Glezer & Amitay (2022)). Owing to their compactness, low power requirements, and ability to produce significant control authority without continuous mass injection, SJs have been extensively investigated for a wide range of engineering applications. These include boundary-layer separation control, film cooling of turbine blades, heat transfer enhancement, mixing augmentation, and jet vectoring in aerodynamic and thermal systems (Feero et al. (2015); Xia et al. (2014)). Based on their geometric configuration and interaction with nearby surfaces, synthetic jets are commonly classified as free synthetic jets (FSJs), impinging synthetic jets (ISJs), and offset synthetic jets (OSJs). For FSJs, which issue into quiescent surroundings without a nearby wall, and ISJs, which impinge perpendicularly onto a surface, the flow characteristics have been extensively studied over a wide range of Reynolds numbers (Xia et al. (2014); Li et al. (2025)). In contrast, OSJs are issued laterally at an offset distance from a nearby wall, resulting in asymmetric entrainment which induces the Coandă effect that draws the jet toward the surface. The attached jet develops into a wall synthetic jet further downstream. Unlike FSJs and ISJs, the influence of Reynolds number on OSJ evolution is rare in the open literature and remains poorly understood.

A schematic of the salient features of a three-dimensional (3D) OSJ is shown in Figure 1. The jet issues from a circular orifice of diameter d with centerline velocity U_{cl}, positioned at a nondimensional offset height G/d above the wall. During each actuation cycle, vortex rings are generated at the nozzle exit, convects downstream while entraining the surrounding fluid. Due to Coandă effect, the jet bends and attaches to the wall at the attachment point x_{ap} to initiate the wall synthetic jet region. The flow characteristics of the OSJ is strongly influenced by the Reynolds number ($Re = \overline{U}_J d/\nu$), Stokes number $\left(S = \sqrt{2\pi f d^2/\nu}\right)$, the stroke length $(L_o = \overline{U}_J/f)$, nozzle geometry and the offset height ratio G/d (Hammond et al. (2025);Cyrus et al. (2025)), where $\overline{U}_j$ is the average jet exit velocity during the expulsion phase, ν is the fluid kinematic viscosity, and f is the actuation frequency. However, these parameters have not been extensively investigated, compared to FSJ.

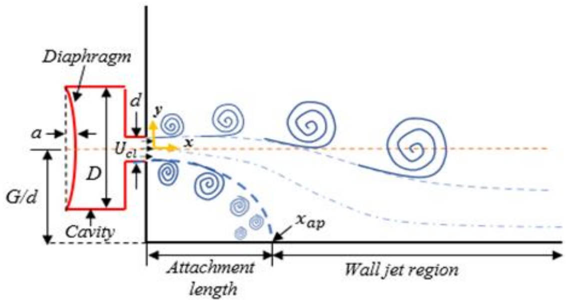

Figure 1. A schematic of an offset synthetic jet attaching to a wall.

Extensive studies on FSJs have demonstrated that Reynolds number and stroke length play a dominant role in determining jet spreading rates, vortex ring coherence, transition to turbulence, and entrainment characteristics. Xia et al. (2014) studied circular synthetic jets at low Reynolds numbers and identified three distinct formation regimes governed jointly by the Reynolds and Stokes number: no-jet formation, jet flow without vortex roll-up, and jet flow with coherent vortex roll-up. Increasing Re was found to promote the transition from non-rolling to rolling vortex structures in the near field, accelerate the onset of shear-layer instability, and enhance downstream vortex convection velocity. Li et al. (2025) investigated the effects of Reynolds number ($Re = 164 - 1308$) and stroke ratio ($L_o = 3.2, 4.8, 6.4$) on FSJ, and found that increasing Re promotes earlier vortex deformation, pairing, and breakdown, and enhances jet spreading and turbulence production.

Existing 3D OSJ studies have predominantly focused on the influence of geometric parameters on jet attachment behavior, vortex dynamics, and near-wall flow characteristics. To the authors' knowledge, Hammond et al. (2025) provided the first 3D characterization of 3D OSJs, employing improved delayed detached eddy simulations (IDDES) to investigate the effects of offset height ratio ($G/d = 1 - 4$) at a fixed $Re = 565$. They found that increasing G/d delays the attachment point, modifies vortex evolution by reducing spanwise stretching and vorticity redistribution, thereby significantly affecting near-wall mixing and turbulent kinetic energy distribution. Concurrently, Cyrus et al. (2025) examined the influence of nozzle geometry (circular, square, and rectangular orifices) on evolution of OSJ at $G/d = 2$ and $Re = 580$ using IDDES. Their findings showed that all jets attached to the wall due to the offset height ratio used, while rectangular nozzles produced earlier attachment points and pronounced axis-switching compared with circular and square geometries. Despite these advances, the Reynolds number has been used as a fixed parameter in both studies; therefore, its systematic influence on OSJ vortex dynamics, wall attachment, and turbulence statistics is not well understood.

The present study aims to address this gap by investigating the effects of Reynolds number on the unsteady flow characteristics and 3D vortex dynamics of OSJs using IDDES. Five Reynolds numbers, $Re = 280, 570, 840, 1000,$ and 1230, are examined at a fixed offset height ratio of $G/d = 2$. The corresponding nondimensional stroke lengths are $L_o/d = 3.65, 7.42, 11.02, 13.17,$ and 16.08, respectively.

NUMERICAL SECTION

The numerical simulations were performed using the finite volume solver STAR-CCM+. IDDES with $k - \omega$ SST model as the Reynolds-averaged Navier–Stokes (RANS) closure was used. The IDDES framework was selected for its demonstrated capability in resolving unsteady, 3D vortex dynamics in wall-bounded and separated turbulent flows at lower computational cost than wall-resolved large-eddy simulation (LES) (Spalart et al. (2006)). By transitioning seamlessly from RANS in attached near-wall regions to LES in separated and shear-dominated regions, IDDES is well suited for capturing the complex vortex-wall interactions and turbulence production mechanisms characteristic of OSJs, as also demonstrated in previous studies (Hammond et al. (2025), Cyrus et al. (2025)).

Following the configuration of Hammond et al. (2025), the synthetic jet actuator (SJA) was modeled with a cavity of diameter $D = 30.8\,mm$ and height $H = 10\,mm$, a neck of diameter $d = 2\,mm$ and height $h = 10\,mm$. The quiescent environment was modeled as a cubic duct of length $50d$ on each side, as shown in Figure 2. A pressure outlet condition was applied at the duct exit, while the SJA walls and all other surfaces were specified as no-slip. The computational domain was discretized using a structured multi-block hexahedral mesh, with grid refinement applied in the region of the jet orifice and adjacent wall region (Figure 2). The SJA diaphragm motion was modelled using a user-defined displacement function, similar to Hammond et al. (2025).

$$s = a\left(1 - \frac{r}{r_o}\right)^2 sin(2\pi f t) \tag{1}$$

where r_o is the cavity radius, and r is the radial position of each grid. The simulations were performed for a fixed offset height ratio of $G/d = 2$ and actuation frequency of $f = 300\,Hz$. However, the actuation amplitude of the diaphragm of the SJA was varied at $a = 18, 32, 46, 54$ and $64\,\mu m$ to obtain Reynolds numbers of $280, 570, 840, 1000,$ and 1230, respectively, hereafter denoted as $R280, R570, R840, R1000$ and $R1230$, respectively. The corresponding centerline velocity values are $U_{cl} = 3.75, 4.60, 11.37, 13.50$ and 16.50. The second-order upwind convection spatial discretization scheme and implicit second-order temporal discretization scheme were used with a time step of $2.5 \times 10^{-6}\,s$, resulting in Courant–Friedrichs–Lewy (CFL) numbers ranging from 0.28 to 0.66 across the Reynolds number cases. Convergence was assessed through residual monitoring, with a minimum threshold criterion of 10^{-6}. For each test case, instantaneous, phase-averaged and time-averaged data were collected after two flow-through cycles and over twelve flow-through cycles, corresponding to 60 actuation cycles.

A mesh sensitivity study was conducted to ensure the numerical accuracy and grid independence of the present IDDES simulations. Three mesh resolutions were evaluated at $Re = 840$: coarse (4.04×10^6 cells), medium (6.84×10^6 cells), and fine (12.24×10^6 cells). As summarized in Table II, the centerline exit velocity and decay rates exhibit monotonic convergence with decreasing numerical uncertainty, with less than 0.5% difference between the medium and fine grids. Additional comparisons of phase-averaged velocity and turbulent kinetic energy profiles at $x/d = 7$ showed close agreement between the medium and fine meshes, however, these results are not shown for brevity. Consequently, the medium grid was adopted for all Reynolds number cases, providing an optimal balance between accuracy and computational efficiency.

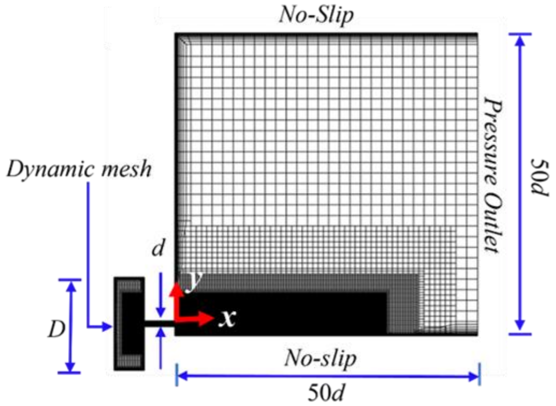

Figure 2. Computational domain and boundary conditions.

Table 1. Summary of mesh independence test

Grid	Cell count	$U_{cl}(m/s)$	Uncertainty (%)	n
Coarse	4.04	11.21	–	0.78
Medium	6.84	11.37	0.16	0.84
Fine	12.24	11.43	0.06	0.85

The numerical methodology was validated against the hot-wire anemometry measurements of Feero et al. (2015), obtained at a comparable Reynolds number and nondimensional stroke length. Radial profiles of the phase-averaged streamwise velocity at the jet exit show good agreement between the simulated and experimental results across both expulsion and ingestion phases (Hammond et al. (2025)). This provides confidence in the fidelity of the SJA model for the present simulations.

RESULTS AND DISCUSSION

Phase-averaged flow

Figure 3 presents the 3D vortex structures at the peak expulsion phase ($\theta = 90°$), visualized using iso-surfaces of the normalized Q-criterion and colored by the corresponding phase-averaged spanwise vorticity. For brevity, $R840$ and $R1000$ are not shown in the figures, as their flow characteristics closely resemble those of $R570$ and $R1230$, respectively. At the lowest Reynolds number ($R280$), the expelled vortex rings are highly coherent and axisymmetric downstream due to interaction with the wall. The limited jet momentum suppresses shear-layer instabilities, allowing viscous diffusion to dominate the vortex evolution (Li et al. (2025)). Consequently, the vortices attenuate rapidly, and the vortex rings exhibit restricted downstream penetration. As the Reynolds number increases to $R570$, the flow transitions into an intermediate regime characterized by strengthened vortex rings that convect farther downstream while largely preserving their coherence. However, the onset of wall interaction introduces asymmetry in the vortex structures. At $R840$, the vortex-ring structures undergo pronounced elongation and deformation. The increased jet momentum amplifies shear-layer roll-up and promotes stronger interaction between the vortex rings and the wall. These effects destabilize the coherent ring structure, leading to significant distortion and fragmentation. The flow in this regime exhibits transitional turbulence, with energy cascading from large-scale coherent structures toward smaller-scale vortical motions. At higher Reynolds numbers ($R1000$ and $R1230$), the vortex-ring structures rapidly disintegrate into a small-scale worm-like structures. Strong wall interaction, coupled with intensified shear-layer instability, accelerates vortex breakdown and suppresses the persistence of the ring coherence.

The phase-averaged spanwise vorticity contours present in Figure 4(a-d) show the formation and downstream evolution of the counter-rotating vortex pairs (CVPs) generated during peak expulsion. For $R280$, alternating regions of positive and negative vorticity appear immediately downstream of the jet exit due to the roll-up of the inner and outer shear layers. The CVPs remain relatively compact but decay rapidly downstream. For $R570$, the CVPs become more pronounced and persist farther downstream compared to $R280$, indicating stronger shear-layer roll-up and enhanced vortex convection.

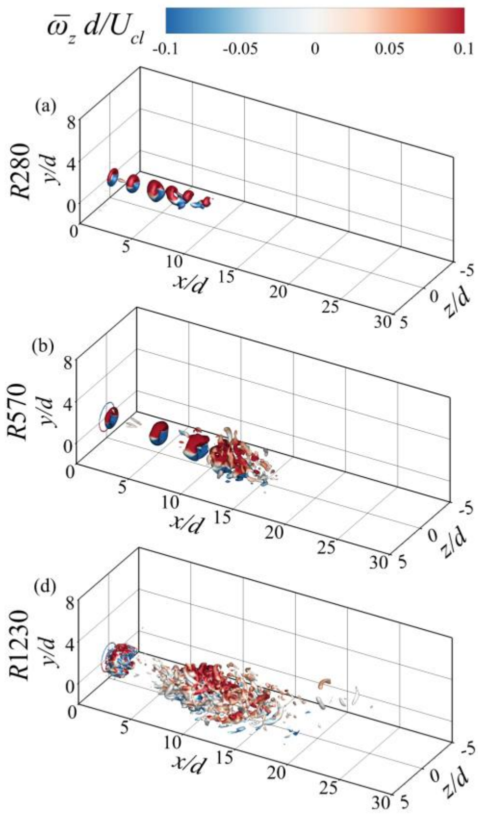

Figure 3. Iso-surfaces of phase-averaged vortical structures educed using normalized Q-criterion ($Q* = Q(d/U_{cl})^2 = 0.008$) coloured with normalized phase-averaged spanwise vorticity at peak expulsion.

At $R840$, the CVPs are less compact and the vorticity field spreads both downstream and in the wall-normal direction. While the initial roll-up near the jet exit is evident, the structures gradually lose coherence beyond $x/d \approx 5$. For the higher Reynolds number cases ($R1000$ and $R1230$), the alternating vortex rings dissipate rapidly and transition into a broader region of weaker distributed vorticity ($x/d \gtrsim 5$), indicating enhanced mixing at higher Reynolds numbers.

Figure 5 shows the phase-averaged Reynolds shear stresses ($\overline{uv}/U_{cl}^2$) at peak expulsion. Two distinct growth regions are observed. The first is a near-field region generated by shear-layer roll-up and vortex-ring formation, and the second is a downstream region ($x/d \geq 3$) associated with the vortex evolution and wall interaction. $R280$, however, is an exception, showing only the downstream growth with weak stresses confined near the jet axis. At $R570$ and $R840$, stronger alternating regions of positive and negative stress emerge, indicating stronger vortex interactions and enhanced mixing. In the higher Reynolds number cases ($R1000$ and $R1230$), the near-field stresses become stronger, while the downstream stresses expand significantly. The distribution in $R1000$ and $R1230$ is qualitatively similar, with large alternating positive and negative regions dominating the shear layers.

Mean flow and velocity decay

Contours of the time-averaged normalized streamwise velocity shown in Figures 6(a–d) reveal the effects of Reynolds number on the mean flow evolution. The isopleth of $U/U_{cl} = 0.01$ is shown on the contours to indicate the interface of the synthetic jets and the ambient fluid.

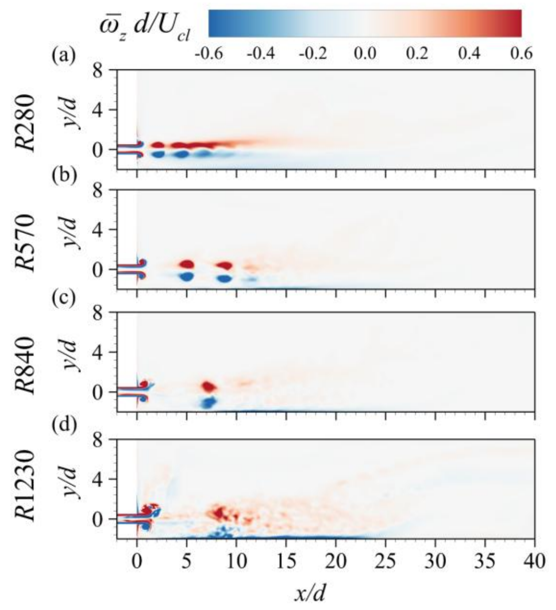

Figure 4. Contours of normalized phase-averaged vorticity ($\overline{\omega_z} d/U_{cl}$) at the symmetry plane.

At $R280$, the attachment point, determined as the streamwise location where the isopleth $U/U_{cl} = 0.01$ first intersects the wall, occurs at $x_{ap} = x/d \approx 8$. Increasing the Reynolds number, the attachment points progressively shift upstream to $x/d = 7$ for $R570$ and $R840, x/d = 6$ for $R1000$, and $x/d = 5.5$ for $R1230$. The reduction in attachment points highlights the role of jet momentum in enhancing entrainment. Concurrently, the potential core length of the jet, defined as the region over which the jet centerline velocity remains within 95% of its peak exit value, reduces with increasing Reynolds number, indicating enhanced mixing and a more rapid transition to turbulence. At $R280$, the potential core length extends to $x/d \approx 7$, and increases to $x/d = 10$ for $R570$ after which it significantly decreases to $x/d = 3$ for $R840 - 1230$. This non-monotonic behaviour is driven by enhanced jet momentum at $R570$, which sustains coherent jet development. At higher Reynolds numbers, however, intensified instability and stronger wall interaction promote jet core shortening.

The decay of the OSJ is characterized using profiles of the maximum streamwise mean velocity (U_m/U_{cl}) for the different Reynolds number cases, as shown in Figure 7.

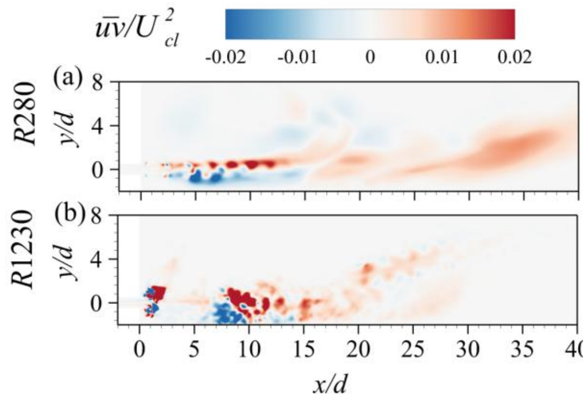

Figure 5. Contours of phase-averaged normalized turbulent kinetic energy and Reynolds shear stress at peak expulsion at the symmetry plane.

The profiles of U_m/U_{cl} exhibit a rapid increase from the orifice exit to a local peak in the near-field region, followed by a gradual decay with increasing streamwise distance. Following previous synthetic jet studies (Hammond et al. (2025)), a power-law, $U_m/U_{cl} \propto (x/d)^{-n}$ where n is the decay rate, was fitted from the end of the potential core of each case to capture the decay region. The resulting decay exponents are $n = 1.3, 0.98, 0.93, 0.73$ and 0.85 for $Re = 280, 570, 840, 1000$ and 1230, respectively. The decay rate decreases monotonically with increasing Reynolds number up to $R1000$, and marginally increases for $R1230$, which may be attributed to earlier interaction with the wall at $R1230$.

Figure 8 presents contours of the wall shear stress, τ_w, for $R280$, $R840$ $R1230$, providing insight into the near-wall momentum transfer induced by the impingement and convection of vortex rings. For brevity, $R840$ and $R1000$ are not shown in the figures, as their flow characteristics closely resemble those of $R570$ and $R1230$, respectively. At $R280$, τ_w is weak and localized, indicating limited near-wall momentum transfer and weak influence of vortex rings on the wall. As the Reynolds number increases, the wall shear stress distribution becomes stronger and spreads further downstream. At $R840$ and higher, the τ_w distribution becomes broader, consistent with spanwise redistribution of the vortical structures (Figure 3). At $R1230$, τ_w forms an extended downstream region up to $x/d \approx 20 - 25$, indicating sustained near-wall momentum transfer associated with more smaller structures near the wall (Figure 3).

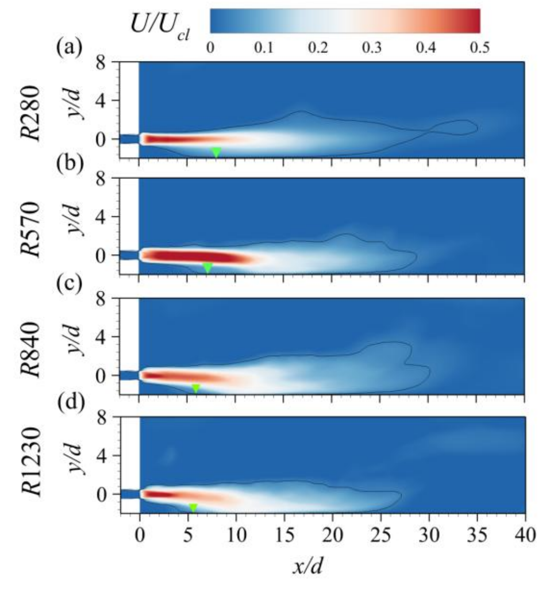

Figure 6. Contours of normalized time-averaged streamwise velocity (U/U_{cl}) at the symmetry plane.

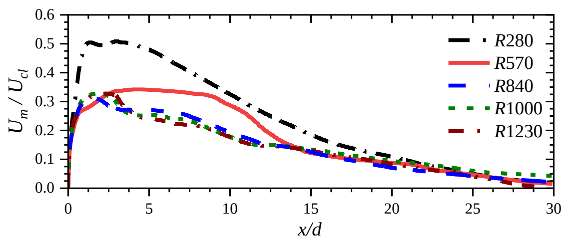

Figure 7. Streamwise evolution of the maximum mean velocity.

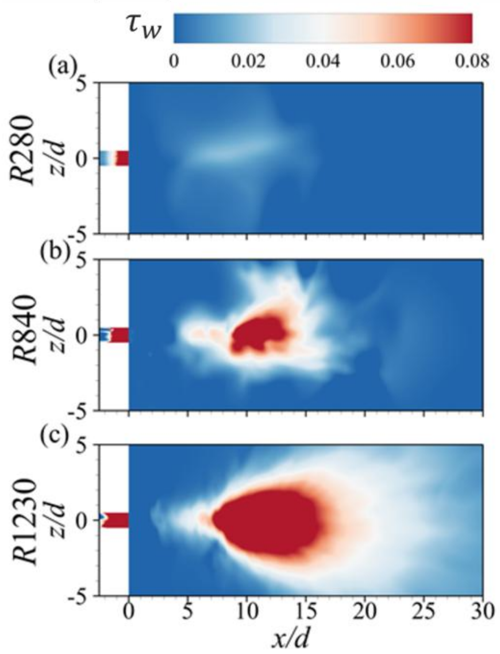

Figure 8. Contours of time-averaged wall shear stress.

Turbulent/non-turbulent interface

The turbulent/non-turbulent interface (TNTI) in the OSJs is examined to characterize entrainment and mixing mechanisms. Following the interfacial-layer framework of da Silva et al. (2014) for steady jets, the TNTI consists of a thin viscous superlayer separating rotational and irrotational regions, where entrainment occurs through small-scale viscous diffusion (nibbling), while large-scale engulfment is associated with coherent vortical motions penetrating the interface. In the present study, the TNTI was identified using the normalized vorticity criterion, where regions satisfying

$$|\omega_z d/U_{cl}| > \omega_{th} \tag{2}$$

were classified as turbulent, with a prescribed threshold value of $\omega_{th} = 0.02$, consistent with established TNTI detection thresholds (Shadkam et al. (2025)). The intermittency factor, defined as the time-averaged probability of turbulence, was computed as

$$\gamma(x,y) = \frac{1}{N}\sum_{n=1}^{N} I_n\,(x,y) \tag{3}$$

where N is the number of instantaneous flow fields and $I_n(x,y)$ is a binary indicator function given by

$$I_n(x,y) = \begin{cases} 1, & |\omega_z d/U_{cl}(x,y,t_n)| > \omega_{th} \\ 0, & |\omega_z d/U_{cl}(x,y,t_n)| \le \omega_{th} \end{cases} \tag{4}$$

Figure 9 presents a representative instantaneous TNTI structure in the wall synthetic jet region of the OSJ for $R1230$, which is qualitatively similar to the other test cases. The contour highlights the turbulent core, surrounded by an irrotational region separated by the convoluted TNTI. The near-wall region exhibits high vorticity and intense mixing, while the outer region remains essentially irrotational. The interface geometry is characterized by its instantaneous height y_i and local inclination angle θ_i, which quantify wall-normal displacement and deformation induced by entrainment and coherent structures.

Figure 10 presents the TNTI characterized using the intermittency factor, γ, where $\gamma = 1$ denotes fully turbulent flow and $\gamma = 0$ corresponds to non-turbulent fluid. The blue line indicates the mean TNTI. At $R280$, a thin turbulent region ($\gamma \approx 1$) is confined close to the wall for $x/d \lesssim 10$, beyond which isolated turbulent patches appear intermittently at larger wall-normal distances up to $y/d \approx 5-6$. These patches correspond to the passage of coherent vortex rings, which periodically engulf ambient fluid as they convect downstream. The TNTI exhibits sharp wall-normal excursions between $x/d \approx 10-20$ before settling back toward the wall as the vortex rings dissipate and the jet attaches. With increasing Reynolds number, the TNTI progressively smoothens and the turbulent region broadens, reflecting the transition from intermittent coherent-structure entrainment toward a continuous turbulent process driven by vortex breakdown and shear-layer instability. At $R1230$, $\gamma \approx 1$ occupies a broad, continuously turbulent region extending to $y/d \approx 2-3$ across the full downstream extent of the domain. The TNTI rises gently and steadily with streamwise distance, exhibiting none of the intermittent excursions characteristic of $R280$. The elevated γ below $y/d = 0$ confirms strong wall attachment and sustained near-wall turbulence, leading to more spatially continuous mixing in the near-wall region.

Figure 11 presents the conditionally-averaged profiles of streamwise velocity (U/U_{cl}) and turbulent kinetic energy (tke/U_{cl}^2) at six streamwise locations ($x/d = 4-20$). Here $(y-y_{tnti})/d < 0$ denotes the turbulent region, while $(y-y_{tnti})/d > 0$ the non-turbulent region. Conditional averaging relative to the TNTI is applied to isolate the interfacial dynamics and mitigate the smoothing effects of large-scale intermittency inherent in classical time- or space-averaged statistics (da Silva et al. (2014)). At $R280$, the proximity of both U/U_{cl} and tke/U_{cl}^2 peaks to the interface suggests that large-scale coherent structures contribute directly to intense interfacial shear and momentum exchange. At higher Reynolds numbers ($R570-R1230$), the peak locations shift toward the turbulent side and near the wall, attributed to the earlier reattachment and development of the wall synthetic jet. Here, large-scale engulfment becomes less dominant, while the outer non-turbulent side of the TNTI continues to be governed by small-scale viscous diffusion, consistent with the intermittency field (Figure 10) and the evolution of vortical structures (Figure 3).

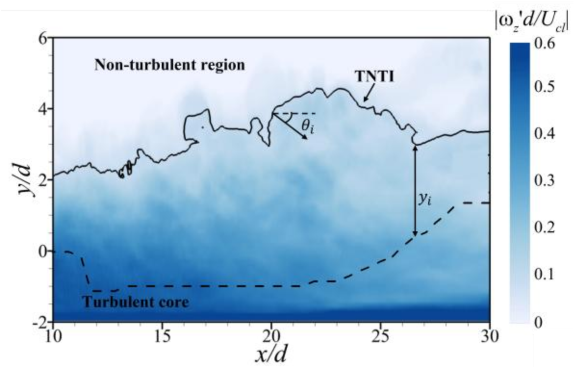

Figure 9. Instantaneous flow field of the TNTI identified using a vorticity-based criterion.

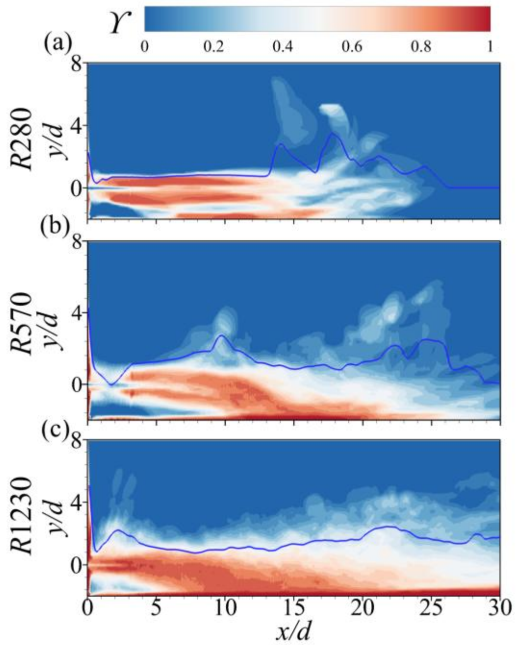

Figure 10. Contours of the intermittency factor (γ) at the symmetry plane. The blue line denotes the mean TNTI location.

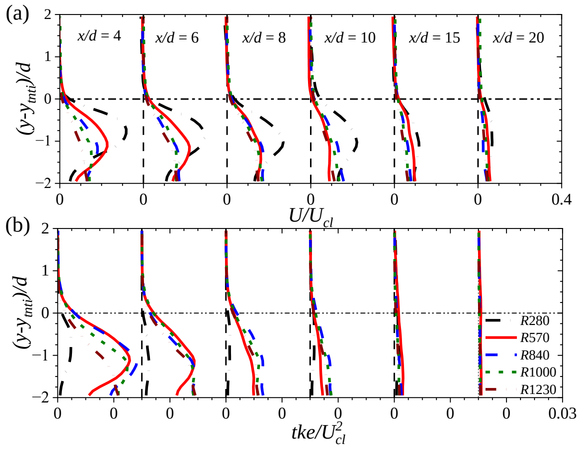

Figure 11. Conditional averages of (a) normalized streamwise velocity (U/U_{cl}) and (b) normalized turbulent kinetic energy (tke/U_{cl}^2). The horizontal dashed line marks the TNTI location.

CONCLUSION

The effect of Reynolds number on the unsteady flow characteristics and 3D vortex dynamics of an offset synthetic jet at $G/d = 2$ was investigated using IDDES for five Reynolds numbers, $Re = 280, 570, 840, 1000$, and 1230. Increasing Reynolds number promotes a transition in vortex dynamics from laminar-like flow at $R280$, characterized by highly coherent, nearly axisymmetric vortex rings that decay rapidly. At $R570$ and $R840$, a transitional regime emerges, where vortex structures progressively lose coherence and undergo increasing deformation due to intensified shear-layer instability and vortex–wall interaction. At $R1000$ and $R1230$, the flow becomes fully turbulent, characterized by rapidly disintegrating small-scale worm-like structures influenced by strong shear-layer instability and enhanced vortex–wall interaction. The wall attachment points shifts progressively upstream with increasing Reynolds number, from $x_{ap} \approx 8$ at $R280$ to $x_{ap} \approx 5.5$ at $R1230$. The streamwise velocity decay decreases with increasing Reynolds number from $n = 1.3$ at $R280$ to $n = 0.73$ at $R1000$, with a slight increase to $n = 0.85$ at $R1230$. TNTI analysis of the OSJs showed that increasing Reynolds number leads to a more spatially distributed turbulent field. At $R280$, turbulence is confined to thin regions associated with coherent vortex-ring passage. With increasing Reynolds number, these regions become more continuous, reflecting progressive vortex breakdown. At $R1000$ and $R1230$, the turbulent field is more uniformly distributed, particularly in the near-wall region, consistent with sustained turbulence and enhanced mixing. Conditional averaging reveals sharp gradients across the TNTI, with turbulence peaking near the interface at $R280$ and shifting toward the turbulent core and near the wall as Reynolds number increases.

REFERENCES

Cyrus, A., Hammond, K. N. D., & Essel, E. E. (2025). Effects of Nozzle Geometry on Turbulent Characteristics of 3D Offset Synthetic Jets. In *ICHMT Digital Library Online*. Begel House Inc.

da Silva, C.B., Hunt, J.C.R., Eames, I. & Westerweel, J. (2014). Interfacial layers between regions of different turbulence intensity. *Annual Review of Fluid Mechanics*, 46, 567–590.

Feero, M. A., Lavoie, P., & Sullivan, P. E. (2015). Influence of cavity shape on synthetic jet performance. *Sensors and Actuators, A: Physical*, 223, 1–10.

Glezer, A., & Amitay, M. (2002). Synthetic jets. *Annual Review of Fluid Mechanics*, 34(1), 503-529.

Hammond, K. N., Sandoval, M. O., Naeem, N., & Essel, E. E. (2025). On the turbulent flow characteristics of wall-attaching synthetic jets at varying offset height ratios. *Physics of Fluids*, 37(11), 115105.

Li, J. F., Zhang, X. B., & New, T. H. (2025). Formation and flow characteristics of low-Reynolds number synthetic jets. *Physics of Fluids*, 37(3), 033631.

Shadkam, A., Pouransari, Z., & Rasam, A. (2025). The turbulent/non-turbulent interface in wall-jets. *Physics of Fluids*, 37(9), 095148.

Spalart, P. R., Deck, S., Shur, M. L., Squires, K. D., Strelets, M. K., & Travin, A. (2006). A new version of detached-eddy simulation, resistant to ambiguous grid densities. *Theoretical and computational fluid dynamics*, 20(3), 181-195.

Xia, Q., Lei, S., Ma, J., & Zhong, S. (2014). Numerical study of circular synthetic jets at low Reynolds numbers. *International Journal of Heat and Fluid Flow*, 50, 456–466.